

ROBERT KOCH INSTITUT



Originally published as:

Alexandrov, T., Lasch, P.
Segmentation of confocal Raman microspectroscopic imaging data using edge-preserving denoising and clustering
(2013) Analytical Chemistry, 85 (12), pp. 5676-5683.

DOI: 10.1021/ac303257d

This document is the Accepted Manuscript version of a Published Work that appeared in final form in Analytical Chemistry, copyright © American Chemical Society after peer review and technical editing by the publisher.

To access the final edited and published work see <http://pubs.acs.org/doi/abs/10.1021/ac303257d>

Segmentation of Confocal Raman Microspectroscopic Imaging Data using Edge- Preserving Denoising and Clustering

Theodore Alexandrov^{1,2,*}, *Peter Lasch*³

¹Center for Industrial Mathematics, University of Bremen, Germany, ²Steinbeis Innovation Center for SCiLS Research, Bremen, Germany, ³“Proteomics and Spectroscopy” (ZBS 6) at the Centre for Biological Threats and Special Pathogens, Robert Koch-Institut (RKI), Nordufer 20, D-13353 Berlin, Germany

KEYWORDS: Biomedical vibrational spectroscopy, Confocal Raman microspectroscopy, Spatial segmentation, Edge-preserving denoising, Cluster analysis, Chemometrics, Tissue analysis

ABSTRACT: Over the past decade, confocal Raman microspectroscopic (CRM) imaging has matured into a useful analytical tool to obtain spatially-resolved chemical information on molecular composition of biological samples and found its way into histopathology, cytology and microbiology. A CRM imaging dataset is a hyperspectral image in which Raman intensities are represented as a function of three coordinates: a spectral coordinate λ encoding the wavelength and two spatial coordinates x and y . Understanding CRM imaging data is

challenging because of its complexity, size, and moderate signal-to-noise-ratio. Spatial segmentation of a CRM imaging data is a way to reveal regions of interest and is traditionally performed using non-supervised clustering which relies on spectral domain-only information. Their main drawback is the high sensitivity to noise. We present a new pipeline for spatial segmentation of CRM imaging data which includes pre-processing in the spectral and spatial domains, and k-means clustering. Its core is the pre-processing routine in the spatial domain, edge-preserving denoising (EPD), which exploits the spatial relationships between Raman intensities acquired at neighboring pixels. Additionally, we propose to use spatial correlation to identify Raman spectral features co-localized with defined spatial regions and confidence maps to assess the quality of spatial segmentation. For CRM data acquired from a mid-sagittal Syrian hamster (*Mesocricetus auratus*) brain cryosections, we show how our pipeline benefits from the complex spatial-spectral relationships inherent in the CRM imaging data. EPD significantly improves the quality of spatial segmentation that allows us to extract the underlying structural and compositional information contained in the Raman microspectra.

INTRODUCTION

The last decade has witnessed an astonishing progress in the field of spectroscopic and spectrometric imaging. Among the optical techniques, vibrational spectroscopic methods like infrared (IR) [1-5] and confocal Raman microspectroscopic (CRM) imaging [4, 6, 7] have seen significant advancements in terms of technology, functionality and spectral quality. Both IR and Raman microspectroscopic imaging provide spatially resolved structural and compositional information on the basis of the vibrational properties of the samples under study and represent in combination with imaging methods a great promise for biomedical applications [6, 8, 9], in

particular for digital staining of histological samples [10] as well as for other applications in microbiology [11, 12], food industry [13], and pharmacy [5, 14-16].

Vibrational spectroscopic imaging methodologies have in common that hyperspectral images (HSI) are produced. These images constitute true 3-dimensional data sets in which the experimental parameter, usually a Raman intensity, or an IR absorbance value, is measured as a function of three independent variables: two spatial coordinates (x,y) and a spectral coordinate, typically the wavelength λ . A HSI can be considered either as a set of spatially resolved spectra, or alternatively as a stack of images in which each image corresponds to a specific wavelength [15-17]. These different views have important implications when developing computational methods for analysis of HSI, since spectral analysis methods as well as image analysis methods are applicable.

Depending on the instrumentation, vibrational hyperspectral imaging experiments can be carried out in different ways [18]. The simplest method is scanning with a single detector system across the surface of a sample in a rasterized manner thus providing a spectrum for each individual spatial (x,y) point. Another method is by using of multi-element detectors such as focal plane array (FPA) detectors. FPA detectors are available for the near and mid-infrared wavelength region and allow parallel acquisition of spectra that significantly reduces the acquisition time. Although the term FPA includes also one-dimensional (“linear”) arrays, it is mostly used to describe two-dimensional (2D) detector arrays [19].

The most obvious difference between hyperspectral, multispectral and color images is the number of wavelength channels. While fluorescence or color images often contain only a limited number of images at discrete “bands” or wavelengths (e.g. three wavelengths in red-green-blue

images), HSI data sets may be composed of up to several thousands of different wavelength images. This advantage is, however, often (but not necessarily) achieved at the expenses of the information content in the spatial domain. The amount of pixels in a spectroscopic dataset usually varies between 10.000 and 100.000 that is significantly less compared to 5-50 megapixels of a state-of-the-art photographic color image.

These facts often predetermine the way how hyperspectral images are analyzed. Instead of classical image analysis methods such as spatial filtering (e.g. sharpening, denoising), edge detection, segmentation and object recognition, HSI analysis methods currently rely predominantly on operations originally developed for point spectroscopy [20]. Vibrational hyperspectral imaging segmentation in biomedical applications is usually conducted via unsupervised spectral clustering [8, 21], spectral unmixing [22-24], or supervised spectra classification [2, 25]. Although these spectra-based methods have been shown to provide insights into the spectral characteristics of spatial regions (e.g. via cluster mean spectra or spectral endmembers), the information contained in the spatial domain is often disregarded. Another drawback of a purely spectra-based segmentation approach is the enhanced sensitivity to noise. Noise may strongly distort signals and diminish the quality the quality of segmentation. For example, we have observed that the signal-to-noise ratio (SNR) strongly affects the results of segmentation: segmentation of noisy HSI may result in spatial cluster segments which are characterized by a high level of granularity with only limited spatial continuity.

The latter observation is important when analyzing Raman imaging data. Compared to IR spectroscopy, Raman spectra exhibit more evident noise. This is a consequence of the fact that Raman spectroscopy relies on a relatively weak optical effect. With cross sections between 10^{-25} and 10^{-30} cm² per molecule [26], Raman inelastic scattering is comparatively weak. Furthermore,

the amount of sample that can be investigated using cutting-edge confocal Raman microspectroscopic instrumentation is at the order of only a few hundred picograms which is about three orders of magnitude less sample amount required for IR microspectroscopic investigations. Both aspects are important to understand why despite new technological advancements such as bright monochromatic laser sources, efficient notch or edge filters, or sensitive CCD detectors, Raman microspectroscopy is often hampered by an only moderate SNR.

We evaluate the proposed pipeline by analyzing the confocal Raman microspectroscopy imaging data of a brain cryosection from a Syrian hamster (*Mesocricetus auratus*). The pipeline makes use of the spectral/spatial relationships present in Raman HSI datasets by combining spatial and spectral processing algorithms. We show that our pipeline significantly outperforms the straightforward spectral domain-only HSI segmentation. The pipeline is based on the approach previously developed for imaging mass spectrometry [27] where it demonstrated excellent image segmentation results. Moreover, we propose methods for interpretation of the produced segmentation maps. First, we propose an approach to identify specific wavelengths showing a high correlation with prominent spatial regions detected by segmentation. Secondly, we propose confidence maps to assess and verify the validity of segmentation maps.

MATERIALS AND METHODS

Tissue from the central nervous system was selected as an ideal test sample for the following reasons. Firstly, the brain anatomy is well-understood. Secondly, brain tissue exhibits a high spectral contrast between the individual anatomical structures, in particular between gray and white matter of the brain and brainstem.

Sample preparation:

The hamster brain sample originated from a female Syrian hamster (*Mesocricetus auratus*). For confocal Raman spectroscopic measurements a mid-sagittal section was produced by cryo-sectioning and thaw-mounting onto a CaF₂ window of 1 mm thickness (Korth GmbH, Altenförde, Germany). Sectioning was carried out by a cryostat (Leica Microsystems, Nussloch/Germany). The cutting temperature was -22 °C and the thickness of the brain slice was 8 µm. To preserve the samples' structural and compositional integrity, freezing water was used as the embedding medium. No organic solvents like xylol or ethanol were used for sample rinsing or washing. The specimens required no further fixation and were kept over weeks in a dry environment at room temperature.

Confocal Raman spectroscopy:

Confocal Raman measurements were carried out in WITec's application laboratory (WITec GmbH, Ulm Germany) by means of a WITec alpha 300R Raman microspectrometer. The instrument incorporated a 300 mm focal length spectrograph (UHTS300 spectrograph) and a 600 lines/mm grating giving a spectral resolution of approx. 4 cm⁻¹. The system was equipped with a frequency-doubled Nd:YAG laser operating at 532 nm. In the exploited Raman microspectrometer, the Rayleigh-scattered light is blocked by an edge filter. Raman back-scattered radiation was focused onto a 100 µm multimode fiber which guided the scattered light to a thermoelectric cooled, back-illuminated CCD detector with 1024×128 pixels from Andor (iDUS DV401A-BV, Andor Technology Plc, Belfast, Ireland). Raman spectra were recorded in the so-called single spectra acquisition mode (no continuous movement of the microscope stage during spectra acquisition) in the spectral range between 349.1 and 3791.9 cm⁻¹. The xyz-scan

stage of the confocal Raman microscope permitted to collect 100×200 Raman spectra consecutively from a sample area of $9249 \times 18247 \mu\text{m}$. The step width in x and y-direction was approx. $9.2 \mu\text{m}$ and the sampling time per Raman spectrum was 3.1 s. An Olympus 50 \times LMPLFLN objective with a numerical aperture (N.A.) of 0.5 and a working distance of 10.6 mm focused the laser light onto the sample.

Spectral pre-processing:

Confocal Raman microspectra were pre-processed by means of the 64-bit version of the CytoSpec software package (<http://www.cytospec.com>, version August 15, 2012) which operated as a pcode toolbox under Matlab R2011a (The Mathworks, Natick, MA). Hyperspectral Raman imaging data in the spectral range of $449\text{--}3500 \text{ cm}^{-1}$ were imported into CytoSpec. The import function included an interpolation routine for converting the dispersive Raman spectra into vectors with an equidistant point spacing of 3.8425 cm^{-1} (i). Spectra were subjected to a quality check (ii) which based on pre-defined thresholds of integrated Raman intensities in the spectral range between 900 and 1750 cm^{-1} . Spectra which did pass the quality check were subsequently subjected to a (iii) cosmic ray removal procedure, (iv) Savitzki-Golay (SG) derivative/smoothing filtering (second derivatives with 5 or 9 smoothing points) and (v) vector-normalization using the spectral region between $700\text{--}1800 \text{ cm}^{-1}$.

Within the context of this study we refer to “raw” spectra as Raman spectra which were pre-processed by steps (i)-(iii), whereas spectrally pre-processed data were additionally subjected to processing steps (iv) and (v).

Spatial pre-processing using edge-preserving denoising:

After spectral pre-processing, the Raman hyperspectral imaging data were subjected to a spatial pre-processing routine, edge-preserving denoising (EPD), which was recently proposed in the context of analysis of hyperspectral MALDI imaging mass spectrometry data [27]. EPD is an operation in the image domain and plays a crucial role in the proposed spatial segmentation pipeline. The aim of EPD is to reduce noise-related pixel-to-pixel variation often unavoidable in Raman microspectroscopic imaging at the same time preserving small spatial features of the wavelength images. Note that the pixel-to-pixel variation is amplified when using the second derivative Raman spectra. For EPD, we used the locally-adaptive edge-preserving image denoising algorithm based on minimizing the total variation (TV) of an image [28]. Informally speaking, TV of a gray-scale image is the sum of absolute differences of intensities at neighboring pixels [29]. Noise increases TV significantly. Penalizing TV when performing denoising obtained recognition for edge-preserving image denosing [30]. Given a gray-scale image, a TV-penalizing algorithm searches for an approximation of this image by simultaneously minimizing its TV. We used the TV-penalizing algorithm which automatically adjusts the local level of denoising [28] implemented as custom Matlab scripts (courtesy Markus Grasmair) with one essential parameter θ encoding the level of denoising taking the values from 0 (no denoising) to 1 (maximal denoising). We applied this algorithm to each wavelength image, thus reducing the noise-related pixel-to-pixel variation of the full Raman HSI dataset.

Cluster analysis for spatial segmentation:

After channel-wise EPD in the image domain, the pre-processed Raman spectra were grouped according to their spectral similarity by means of k-means cluster analysis [31] (KMC); see data

analysis workflow in Supporting figure S1. KMC is a well-known multivariate crisp clustering technique which has shown its usefulness in analysis of Raman or IR microspectroscopic imaging data [21, 32, 33]. The results of spectra clustering were converted into a false-color spatial segmentation map which visualizes clustering assignments of all pixels by coloring them so that the pixels of spectra from the same cluster have the same color. Note that spatially disconnected regions may have the same color. We systematically calculated spatial segmentation maps for numbers of clusters ranging from two to ten and selected those with the best agreement with the anatomy of the brain. For KMC-based spatial segmentation, in-house developed Matlab scripts were employed.

Interpretation of the spatial segmentation maps:

In hyperspectral imaging, the interpretation of the results of clustering is usually carried out by means of spatial segmentation maps (cluster images) and cluster mean spectra. While spatial segmentation maps illustrate the spatial distribution of spectral patterns of a given hyperspectral image, cluster mean spectra are meaningful to demonstrate and interpret spectral differences found between clusters [21].

We propose an alternative, correlation-based approach to extract spatial and/or spectral information from HSI. Given a cluster of spectra, one can define a spatial mask as an image with values of one for cluster member spectra and zero values for all other spectra. Calculation of Pearson's correlation coefficients between such a spatial mask and all original wavelength images prior to EPD allows one to identify those Raman wavelengths ("features") which are correlated, un-correlated or anti-correlated with the given cluster. Note that the degree of

correlation between a given cluster mask and wavelength images is independent on the Raman intensities and thus allows one to detect also Raman spectral features of low intensity.

Additionally, to estimate the quality of the produced spatial segmentation map, we propose confidence maps. We propose to define “confidence” as a mean value of Pearson correlation between a given cluster mask and its three most correlated wavelength images. Visualization of the totality of confidence values on the segmentation map is the confidence map. A confidence map thus highlights clusters of high (or low) confidence, i.e. clusters for which correlated wavelength images exist (or do not exist). We found that this information is of particular importance for interpreting the segmentation map: the spectral information derived from clusters of low confidence should be interpreted with caution. Note that this approach be used for selecting an appropriate level of denoising by comparing confidence maps generated for segmentation maps with several possible levels of denoising. For correlation-based image analysis, in-house developed Matlab scripts were employed.

RESULTS AND DISCUSSION

The main goal of the present study was to develop and evaluate a pipeline for spatial segmentation of Raman hyperspectral images (HSI). The proposed pipeline is based on a combination of a classical image processing operation, edge-preserving denoising (EPD) applied to chemical images of Raman HSI, and unsupervised k-means clustering (KMC) for purely pixel based segmentation. Using this pipeline, we analyzed a confocal hyperspectral Raman imaging dataset collected from a mid-sagittal cryosection of a hamster brain. Our data analysis workflow employed is illustrated in Supporting figure S1.

[FIGURE 1]

Figure 1 shows the anatomy of the rodent brain and brainstem as a schematic mid-sagittal view. The major anatomical regions like the medulla oblongata, pons, hippocampus, thalamus, corpus callosum, or the cerebellum with the cerebellar structures arbor vitae and the cerebellar cortex have been labeled. White matter structures are depicted in red whereas gray matter structures are shown in blue. Examples of brain structures composed mainly of white matter are the corpus callosum, fornix, pons and large areas of the medulla oblongata. White matter forms also a tree-shaped structure inside of the cerebellum, called arbor vitae. Blue colored areas such as the cerebral cortex, the main olfactory bulb, the hippocampus, or the cerebellar cortex denote gray matter structures.

White and gray matter are known to differ by their biochemical composition: whilst gray matter is mainly composed of neuronal bodies, glial cells, neuropil and both myelinated and unmyelinated axons, the cerebellar white matter is formed by lipid-rich components such as myelinated axons.

Spectral differences between the white and gray matter:

Raman spectroscopy can be used to differentiate between white and gray matter structures of the brain [34, 35]. These differences are primarily based on the well-known lipid composition which may vary significantly between different brain structures [36, 37].

Typical Raman spectroscopic differences detected between white and gray matter structures of the hamster cerebellum are illustrated by figure 1. The red spectrum represents a mean Raman spectrum obtained by averaging several tens of manually selected point spectra from the arbor vitae region. To demonstrate the noise level of the raw data, one of the un-processed Raman spectra has been also exemplified (dark red trace). The inset in figure 1 provides an estimate of

the signal-to-noise-ratio (SNR) which has been obtained by calculating the ratio of the maximum Raman intensity in the C-H stretching region (2800 - 3050 cm^{-1}) and the standard deviation of the intensities in the signal-free region between 1900 – 2400 cm^{-1} . The mean spectrum and an exemplary raw Raman spectrum from the granular layer of the cerebellar cortex are shown in blue. Figure 1 demonstrates that both the general shape of the spectral profile and the intensities of lipid-associated Raman bands reflect the gross compositional differences between white and gray matter. The most significant dissimilarities are found in the C-H stretching region, i.e. between 2800 and 3050 cm^{-1} (see table 1 for band assignments). Relatively large differences were detected also in other regions of the Raman spectra: at 1445 cm^{-1} (C-H def.), 1068 cm^{-1} (C-N and C-C str) and at another C-H deformation band near 1303 cm^{-1} (C-H def). Further typical changes were obtained at 548 cm^{-1} (cholesterol), 883 cm^{-1} (choline head group vibration), 1589 cm^{-1} (C=C str) and at 3065 cm^{-1} (C-H str of -C=C-H groups, cf. table 1 for details of band assignments). Although some of the discriminatory Raman signals can be detected only in mean spectra - a consequence of the only moderate SNR of the raw data - the band assignments strongly suggest that the spectral differences are indeed associated with specific distribution patterns of important classes of brain lipids.

[TABLE 1]

[FIGURE 2]

Spatial segmentation maps: Spatial segmentation maps with 7 clusters obtained on the basis of spectral-domain-only pre-processing and unsupervised k-means cluster (KMC) analysis are illustrated in figure 2A. Pre-processing included quality tests, cosmic ray rejection and the application of a second derivative SG smoothing/derivative filter with 5 smoothing points. Prior

to KMC-based image segmentation, filtered spectra were additionally vector-normalized using the Raman intensities in $700\text{--}1800\text{ cm}^{-1}$. According to figure 2A, the pixel based image segmentation procedure produced only incoherent cluster segments with no clear boundaries (possibly a result of noise amplification in the derivative spectra). Obviously, the segmentation using spectra-domain-only methods resulted in spatial masks of high granularity with no, or only limited, spatial continuity. The spatial segmentation maps improved dramatically after applying edge-preserving denoising (EPD) in the image domain, see figure 2B. The sequence and parameters of spectral pre-processing and image analysis procedures were kept fixed to ensure comparability with the instance of figure 2A. According to figure 2B, EPD at a moderate level – $\theta=0.65$ is the recommended value, see [27] – significantly improved the interpretability of the segmentation map by reducing the granularity of the map and by generating coherent cluster regions with well-defined boundaries. Moreover, figure 2B also demonstrates that EPD has led to a better correspondence with the brain anatomy by allowing us to recognize important anatomical structures like the corpus callosum or cerebellar structures.

[FIGURE 3]

A second example that illustrates the influence of the EPD parameter θ on segmentation is given by figure 3. Apart from the parameter θ and the number of smoothing points of the SG filter function (9 instead of 5), all remaining processing parameters and analysis steps were kept identical. Figure 3 shows spatial segmentation maps constructed without EPD pre-processing ($\theta=0$, figure 3A) as well as with EPD pre-processing using weak ($\theta=0.55$, figure 3B), moderate ($\theta=0.65$, figure 3C) and strong ($\theta=0.75$, figure 3D) levels of denoising.

The first conclusion that can be drawn from the segmentation maps of figure 3 is that spatial segmentation on the basis of spectral domain-only pre-processing again resulted in a granular segmentation map with no, or only limited spatial continuity (see figure 3A). Secondly, the computationally increased SNR after stronger spectral smoothing (SG filter function with 9 instead of 5 smoothing points) exerted no noticeable effect on the degree of correspondence between image segmentation and brain anatomy (cf. figures 2A and 3A). Thirdly, the segmentation maps obtained from spectrally and spatially pre-processed data have a higher degree of spatial coherence (see figure 3B-D). Unlike smoothing in the spectral domain, EPD has shown a marked effect on coherence, size and shape of the individual spatial masks: the larger the denoising level θ , the lower the granularity of the KMC spatial segmentation maps.

Comparison of the spectral properties of spatial segments obtained with and without EPD:

A major goal of this study was to elucidate how EPD applied in the spatial domain of Raman HSI affects the spectral information content of spatial segments. For this purpose, we calculated cluster mean spectra using the spatial masks obtained by KMC of spectral-domain-only pre-processed, and of EPD-pre-processed data, respectively. Although these segments are composed by different spectra, we were able to match each cluster obtained without EPD with a cluster obtained with EPD (by comparing their mean spectra). Cluster mean spectra computed from these spatial masks on the basis of raw Raman spectra are provided in figure 4 and illustrate the Raman characteristics of cluster masks obtained without EPD (traces 1, $\theta=0$) and EPD at a moderate level (traces 2, $\theta=0.65$). For both approaches, the most significant Raman spectroscopic differences were found between clusters encoding the spatial masks given by the red (white matter) and yellow color (gray matter, note that the color scheme of figure 4 is

consistent with the schemes used in figures 2 and 3). Furthermore, a detailed comparison of the mean spectra provided in figure 4 was carried out by systematically calculating Euclidean distances between all possible pairs of mean spectra. These analyses revealed an average Euclidean distance of 23,309 (max: 56,004, min: 4,412) for the mean spectra labeled in figure 4 by 1 (no EPD), and of 20,778 (max: 51,491, min: 4,139) for mean spectra obtained on the basis of KMC and EPD of a moderate level (labeled in figure 4 by 2). At the one hand these number suggest that EPD may be the cause of a slight reduction of the spectral distinctness of the spatial masks. On the other hand, as the general pattern of the cluster-specific Raman spectroscopic signatures remains surprisingly consistent (except for the blue cluster), it is even conceivable that these small changes are a result of other factors, such as random initialization of the KMC process. Although it is not possible to decide at the present stage whether the increase of the spectral similarity results from EPD or not, it is beyond any doubt that the suggested EPD-based pre-processing pipeline causes no substantial modifications of the spectral characteristics of spatial masks and thus of their underlying structural and compositional information.

The influence of EPD on the Raman spectra:

In the previous paragraph we have shown that the spectral properties of spatial masks obtained with and without spatial pre-processing (EPD) do not change much. However, we have not yet investigated the direct influence of EPD on the spectral contrast. For this purpose we have manually defined so-called regions of interest (ROIs) which were specified on the basis of the segmentation map from figure 3C. For each ROI, we computed mean, 5%, and 95% percentile spectra, respectively, from the raw Raman data and Raman spectra spatially pre-processed by weak, moderate or strong EPD ($\theta=0.55$, 0.65 or 0.75 , respectively). It is important to emphasize that contrary to the preceding example, the mean and the percentile spectra were obtained on the

basis of identical spatial masks. The results of our analysis are shown in Supporting figure S2. The main observations are as follows: (i) Mean spectra of the various ROI masks are different and exhibit distinct and ROI-specific Raman features. (ii) The effect of EPD onto mean spectra is not visible. (iii) The spectral variance within the ROI masks is largely affected by EPD: the smaller the level of EPD, the larger the spectral variance within the manually defined ROIs, see for example spectra in panel E of Supporting figure S2. In summary, Supporting figure S2 demonstrates that EPD of HSI exerts only negligible effects on the average spectral characteristics of reasonably large region of HSI whereas the spectral variance within such regions is significantly reduced.

[FIGURE 4]

Interpretation of spatial segmentation maps:

When analyzing and interpreting spatial segmentation maps, it is important to address the following points: (i) the question for the optimal number of clusters, (ii) the existence of a fair correlation between the reference (histology) and hyperspectral imaging technique, and (iii) which of the spectral features are specific for a given spatial mask. As for the first point, there is a large body of literature available that helps to determine the optimal number of clusters; see e.g. [38]. The second question can be answered based on an investigator's experience in the reference technique, such as histology or microanatomy.

Below we introduce a correlation-based approach which can be used to address the third question. This technique is based on the calculation of Pearson's correlation coefficients r between a given spatial mask and wavelength images allowing one to find specific wavelengths that are correlated with cluster masks, and therefore with anatomical regions.

[FIGURE 5]

Figure 5 gives an example of a correlation analysis. It shows the spatial mask of the cluster encoded by the red color of figure 2B that was associated with white matter structures of the medulla oblongata, corpus callosum, anterior commissure, and arbor vitae. The correlation analysis revealed high correlation coefficients between this cluster mask and the wavelength images at the following wavelengths: (i) 1442, (ii) 2852, (iii) 2883, (iv) 705, and (v) 1070 cm^{-1} (sorted in descending order according to r). The wavelength images of these Raman intensity features are shown in figure 5B-F. The correlation coefficients range from 0.239 to 0.430 (see inset). Most of the identified Raman features apparently arise from C-H, or C-C vibrational modes. For example, the features at 2852 and 2883 cm^{-1} were previously assigned to the symmetric C-H stretching vibration of methylene groups [35, 39], and a Fermi resonance thereof [35]. In Raman spectra of biomedical samples the C-H stretching (2800–3050 cm^{-1}) region is known to be dominated by contributions from fatty acids of membrane amphiphiles (e.g. phospholipids) and to less extent by amino acid side-chain vibrations [39]. Interestingly, the Raman band with the highest correlation (1442 cm^{-1}) has been assigned to a vibrational mode of $>\text{CH}_2$ (methylene) groups originating from C-H deformations [40]. Thus, the three most correlated Raman features can be associated to vibrations of one and the same functional group. The next two Raman features found by correlation analysis at 1070 cm^{-1} (C-N and C-C stretching vibrations, see table 1 for band assignments) and at 705 cm^{-1} (no band assignment available)

correspond to Raman bands of only weak intensities. The mean spectrum of the analyzed spatial mask (red color) is shown in figure 5G with the found top five correlated Raman features highlighted. It shows that these features are not only correlated with the white matter region but exhibit also certain Raman intensity.

Confidence maps:

To evaluate and interpret the spatial segmentation maps, we computed their confidence maps. The confidence map of the spatial segmentation map from figure 2B shows that white matter structures forming the red and the blue cluster (corpus callosum, arbor vitae, pons, medulla oblongata) exhibit Raman features with a good co-localization to these spatial masks (figure 5H). As the algorithm of obtaining confidence maps does not consider for the presence of anti-correlated features, the gray matter structures often display only low confidence values.

CONCLUSIONS

We have proposed a new pipeline for analysis of confocal Raman microspectroscopy imaging data by means of spatial segmentation combining pre-processing methods in both the spectral and the spatial domains with unsupervised clustering. For a Raman HSI dataset of a mid-sagittal hamster brain section, we could demonstrate that pre-processing in the spatial domain by edge-preserving denoising (EPD) suppressed the pixel-to-pixel variation significantly and led to a superior correlation between brain anatomy and the results of Raman HSI segmentation. While pre-processing by spectral domain-only operations resulted in spatial masks of a high granularity, application of EPD significantly improved the quality of the spatial segmentation. The presented approach is not only valuable to produce coherent spatial segmentation maps, but also shows its strength in establishing true spatial-spectral relationships particularly in

applications where noise plays a major role. The proposed algorithm is considered to be valuable for segmentation of HSI data obtained by various vibrational microspectroscopic techniques such as confocal Raman microspectroscopic imaging, infrared imaging, terahertz imaging, as well as other HSI techniques.

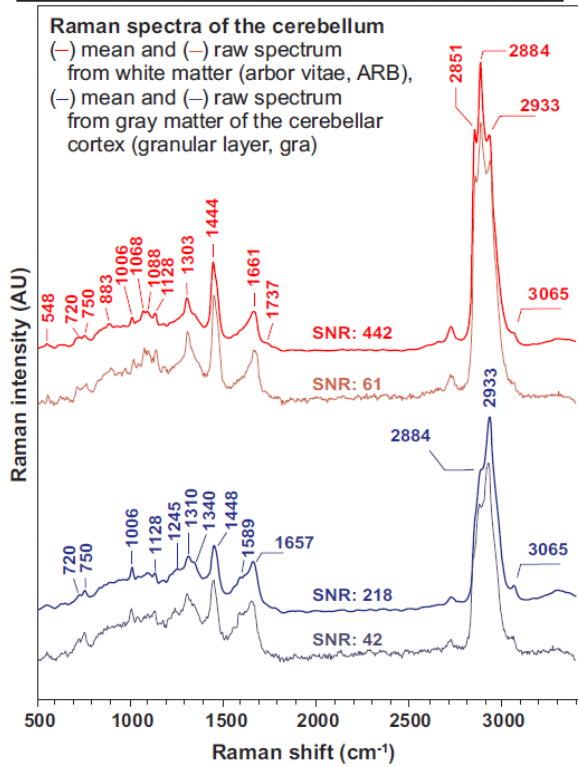
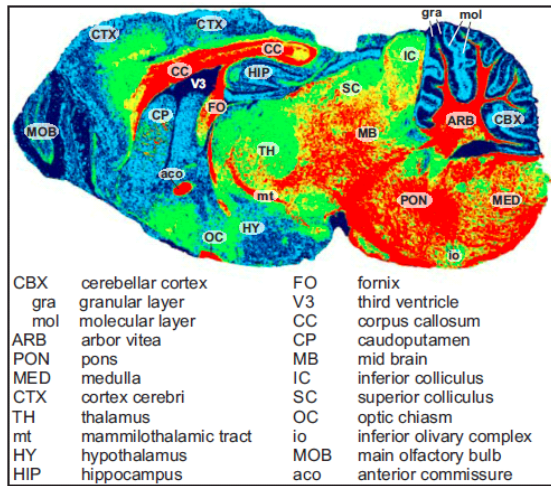


Figure 1. Top panel: Anatomy of the hamster brain (mid-sagittal view, see inset and text for details). Bottom panel: Raman spectra from the hamster cerebellum. Mean spectrum (red) and unprocessed single-pixel Raman spectrum (dark red) of white matter structures (arbor vitae). Mean (blue) and unprocessed single pixel (dark blue) Raman spectrum from the gray matter (granular layer of the cerebellar cortex). The spectra are shifted along the y-axis for clarity; for band assignments see table 1.

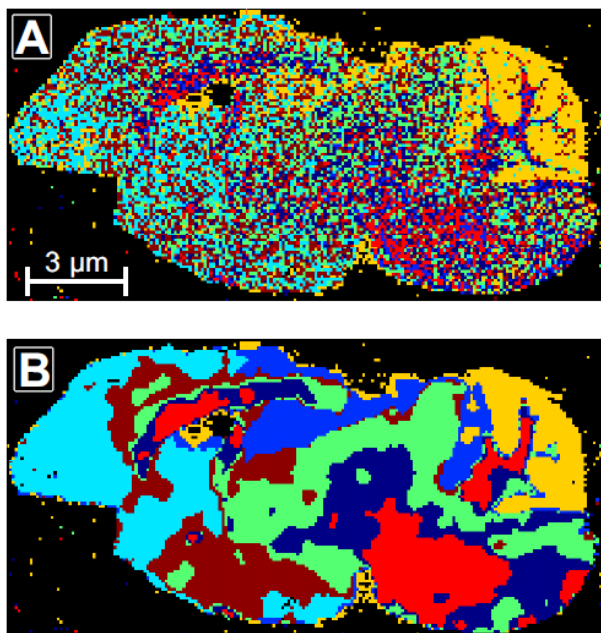


Figure 2. Comparison of HSI segmentation (k-means clustering with 7 clusters) carried out with and without edge-preserving denoising (EPD). (A) spectral domain-only pre-processing (no EPD, $\theta=0$). (B) pre-processing in the spectral and spatial domain, (moderate EPD, $\theta=0.65$). Spectral pre-processing: quality test, cosmic ray removal, Savitzky-Golay (SG) filtering, vector-normalization (SG 2nd derivative/smoothing filter with 5 smoothing points, normalization in the spectral range of 700 and 1800 cm^{-1})

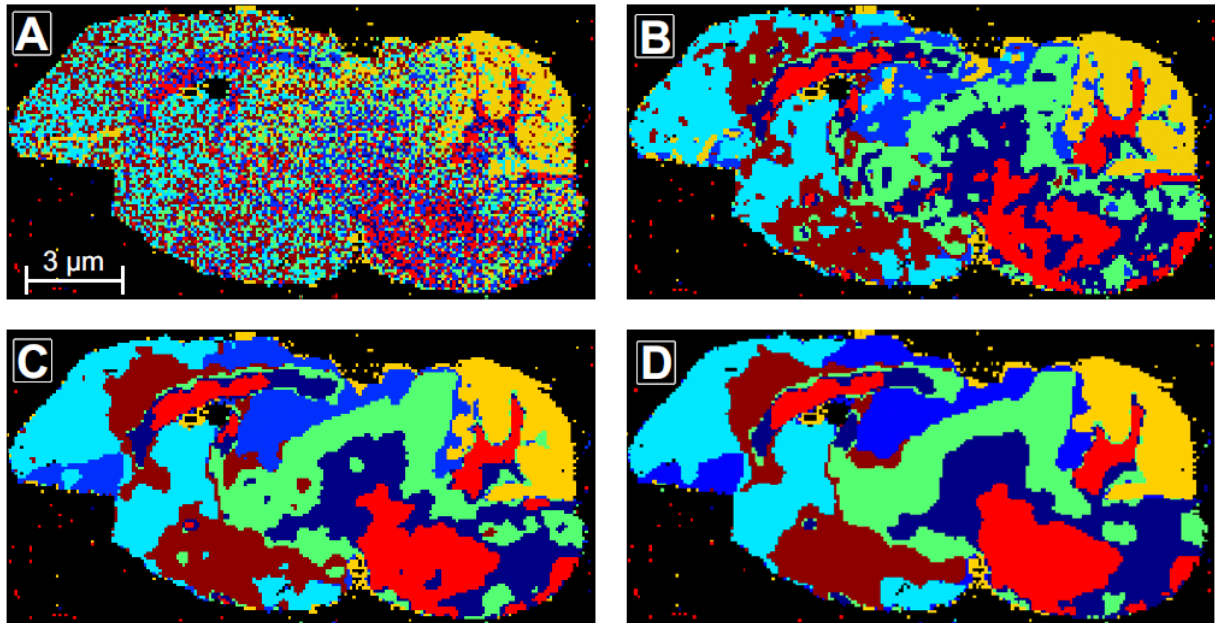


Figure 3. The influence of the degree of EPD on the results of HSI segmentation (k-means clustering, 7 clusters). (A) pre-processing only in the spectral domain (no EPD, $\theta=0$). (B) pre-processing in the spectral and spatial domain (weak EPD, $\theta=0.55$). (C) pre-processing in the spectral and spatial domain (moderate EPD, $\theta=0.65$). (D) pre-processing in the spectral and spatial domain (strong EPD, $\theta=0.75$). Spectral pre-processing: quality test, cosmic ray removal, Savitzky-Golay (SG) filtering, vector-normalization (SG 2nd derivative/smoothing filter with 9 smoothing points, normalization in the spectral range of 700 and 1800 cm^{-1}).

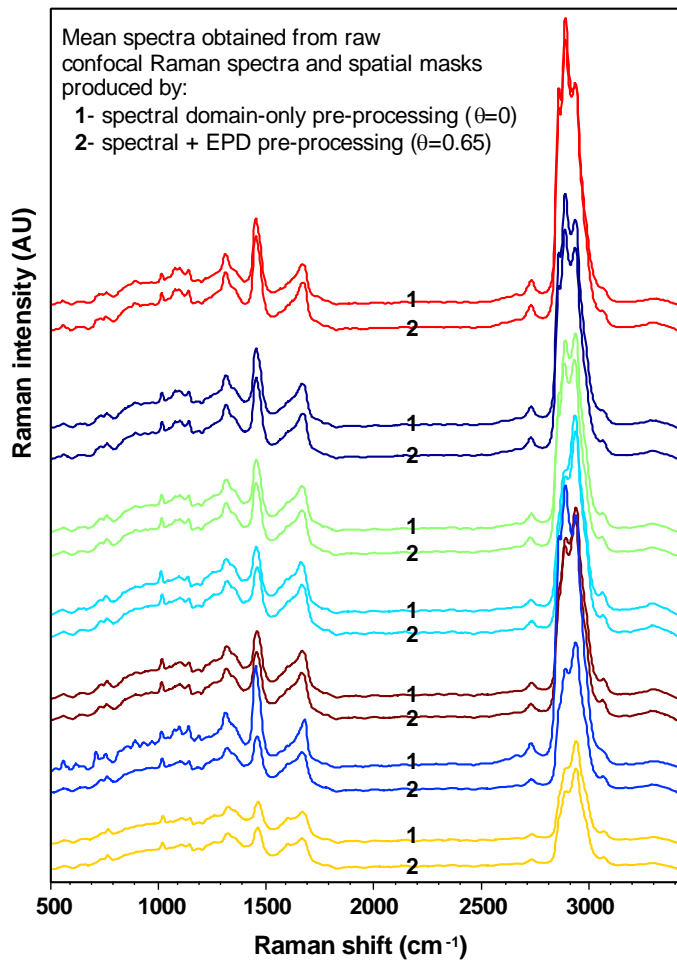


Figure 4. Mean spectra obtained from the spatial masks of figure 2 (note that the color scheme is consistent with the scheme used in figures 2-3). (1) mean cluster spectra obtained from the mask of figure 2A ($\theta=0$, no EPD). (2) mean cluster spectra obtained from the mask of figure 2B ($\theta=0.65$, moderate level of EPD)

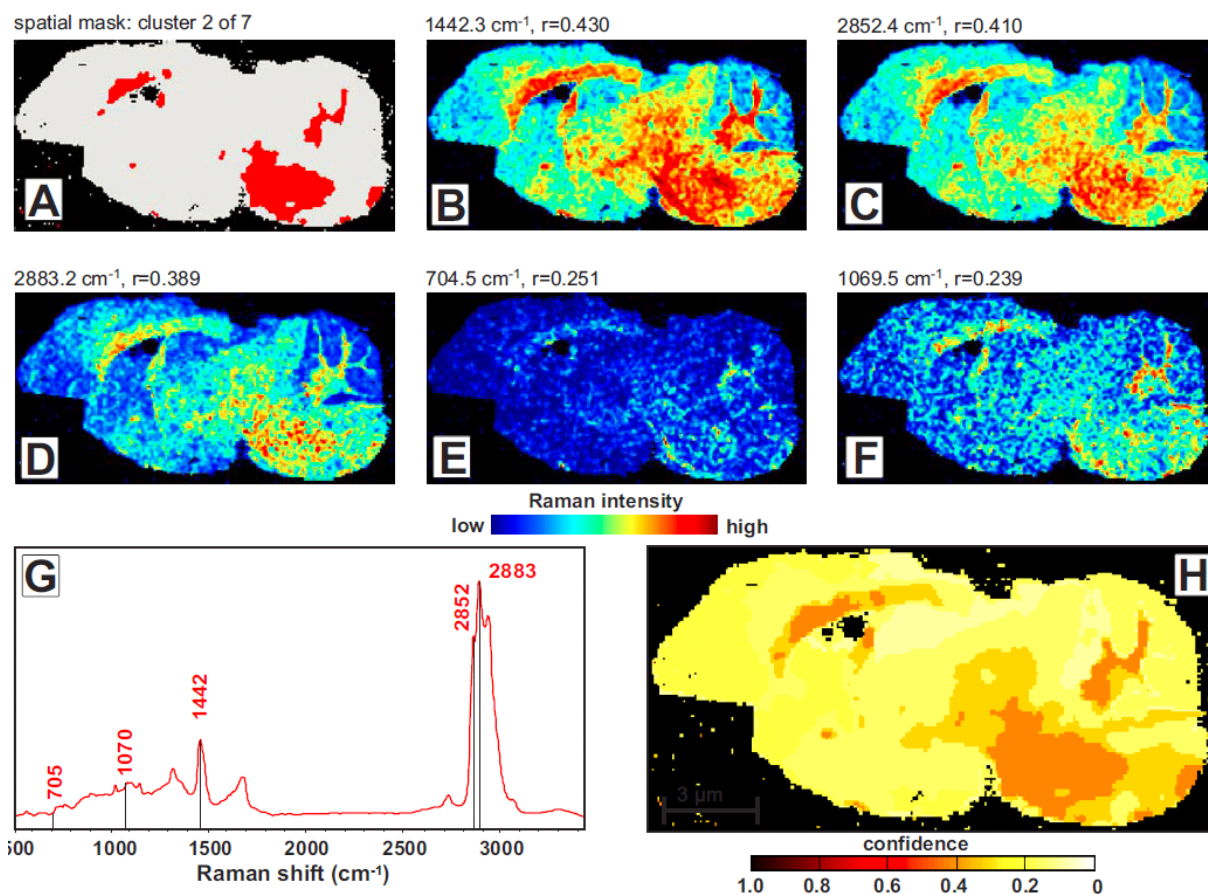


Figure 5. (A) Spatial mask of cluster 2 (red region of figure 2B) obtained by KMC image segmentation (moderate level of EPD, $\theta=0.65$). (B-F) Feature images showing a high correlation with the spatial mask of panel A. The inset of each image shows the wavenumber position of the Raman feature and Pearson's correlation coefficient r . (G) Mean Raman spectrum of the spatial mask of the “red” cluster (red region of figure 2B, see also panel 5A). Spectral features with a high correlation to this mask are indicated. (H) Confidence map for the 7-cluster segmentation approach given by the example of figure 2B (moderate level of EPD, $\theta=0.65$).

Table 1. Raman band assignments. Abbreviations: str = stretching, def = deformation, sy = symmetric, as = antisymmetric (adapted from [35, 39, 41]).

Wavenumber positions [cm ⁻¹]	Putative assignments
548	Chol [35]
720	C-H ₂ def, N ⁺ -(CH ₃) ₃ str (sym) [35]
883	N ⁺ -(CH ₃) ₃ str (asym) [35]
1006	ring breathing (phenylalanine) [39]
1068	C-N and C-C str
1088	PO ₂ ⁻ str, C-O str
1228	CH def
1245	amide III [39]
1310	C-H def
1340	C-H ₂ def
1444	C-H def [35, 39, 40]
1589	C=C str
1657, 1661	amide I [35, 39]
1737	C=O str of esters [39, 40]
2851	C-H str (sy) of >CH ₂ [35, 40]
2884	C-H str (Fermi-Resonance) of >CH ₂ [35, 40]
2933	C-H str (sy) of -CH ₃ [35, 39, 40]
2960	C-H str (as) of -CH ₃ [35]
3010	C-H str (sy) of =CH- [35]
3065	C-H str of (C=C-H) _(arom) [39]

AUTHOR INFORMATION

Corresponding Author

- Phone: +49 421 218 63820, email: theodore@uni-bremen.de

Author Contributions

PL and TA designed the study. PL performed pre-processing of the data. TA produced spatial segmentation maps and provided data for interpretation. PL performed interpretation of Raman features. PL and TA wrote the manuscript.

Funding Sources

The research leading to these results has received funding from the European Union Seventh Framework Programme FP7 under grant agreement 305259.

ACKNOWLEDGMENT
The authors thank Dr. Michael Beekes for providing the hamster brain specimens. We are furthermore thankful to Dr. Thomas Dieing (WITec GmbH, Ulm/Germany) for conducting the confocal Raman measurement of the hamster brain section.

ABBREVIATIONS

CRM, confocal Raman microspectroscopy; EPD, edge-preserving denoising; FPA, focal plane array; HSI, hyperspectral image; IR, infrared; KMC, k-means clustering; MALDI-TOF MS, matrix-assisted laser desorption/ionization time-of-flight mass spectrometry; ROI, region of interest; SG, Savitzky-Golay; SNR, signal-to-noise ratio; THz, terahertz; TV, Total Variation.

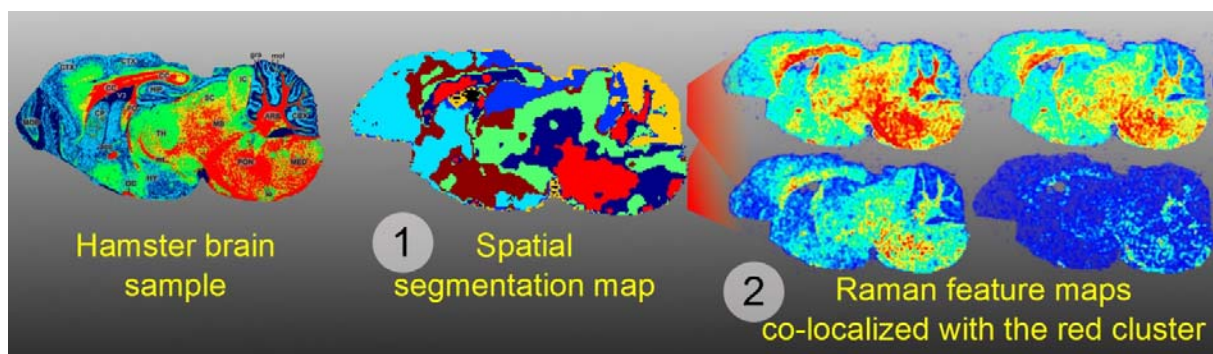
REFERENCES

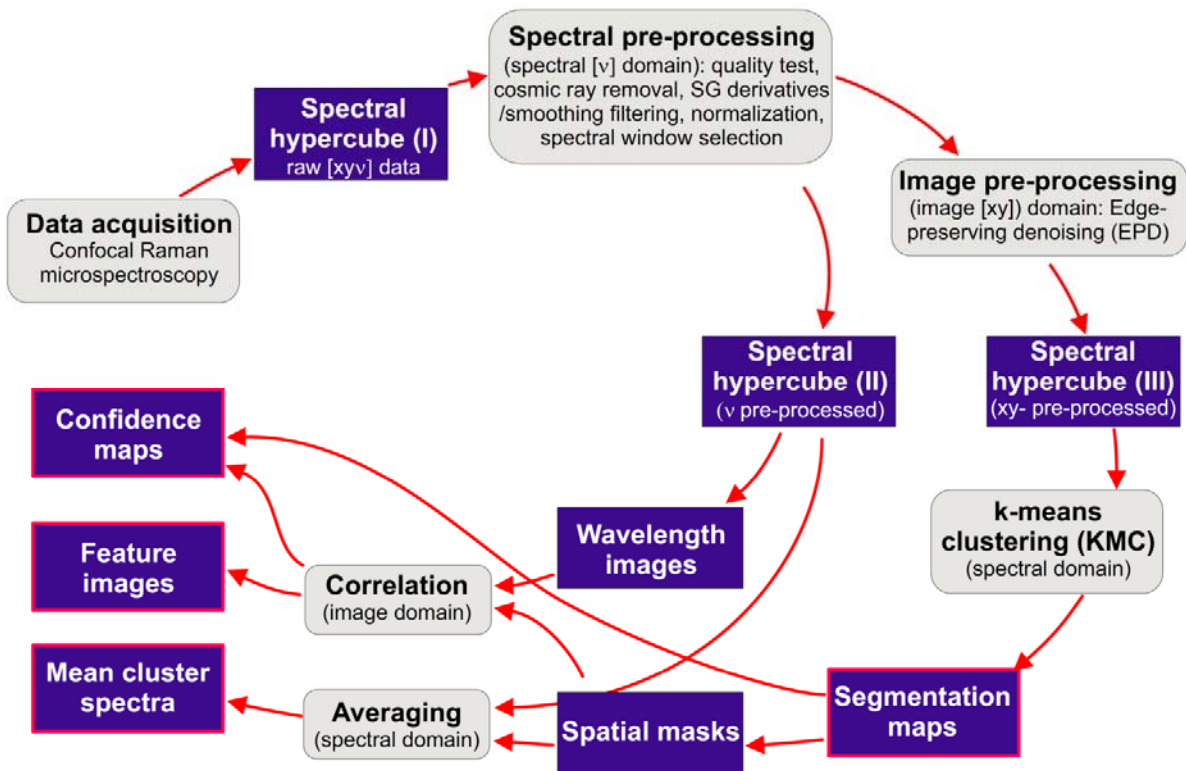
1. Lewis, E.N., et al., *Fourier transform spectroscopic imaging using an infrared focal-plane array detector*. *Anal Chem*, 1995. **67**(19): p. 3377-81.
2. Lasch, P. and D. Naumann, *FT-IR microspectroscopic imaging of human carcinoma thin sections based on pattern recognition techniques*. *Cell Mol Biol (Noisy-le-grand)*, 1998. **44**(1): p. 189-202.
3. Kidder, L.H., et al., *Visualization of silicone gel in human breast tissue using new infrared imaging spectroscopy*. *Nat Med*, 1997. **3**(2): p. 235-7.
4. Salzer, R., et al., *Infrared and Raman imaging of biological and biomimetic samples*. *Fresenius J Anal Chem*, 2000. **366**(6-7): p. 712-6.
5. Kazarian, S.G. and K.L. Chan, *Applications of ATR-FTIR spectroscopic imaging to biomedical samples*. *Biochim Biophys Acta*, 2006. **1758**(7): p. 858-67.
6. Schaeberle, M.D., et al., *Raman chemical imaging: histopathology of inclusions in human breast tissue*. *Anal Chem*, 1996. **68**(11): p. 1829-33.
7. Matthäus, C., et al., *Chapter 10: Infrared and Raman microscopy in cell biology*. *Methods Cell Biol*, 2008. **89**: p. 275-308.
8. Diem, M., S. Boydston-White, and L. Chiriboga, *Infrared Spectroscopy of Cells and Tissues: Shining Light onto a novel Subject*. *Appl. Spectrosc.*, 1999. **53**(4): p. 148A-161A.
9. Lasch, P., et al., *Characterization of Colorectal Adenocarcinoma Sections by Spatially Resolved FT-IR Microspectroscopy*. *Appl. Spectrosc.*, 2002. **56**(1): p. 1-9.
10. Fernandez, D.C., et al., *Infrared spectroscopic imaging for histopathologic recognition*. *Nature Biotechnology*, 2005. **23**(4): p. 469-474.
11. Mossoba, M.M., et al., *Printing microarrays of bacteria for identification by infrared microspectroscopy*. *Vib. Spec.*, 2005. **38**: p. 229-235.
12. Hermelink, A., et al., *Phenotypic heterogeneity within microbial populations at the single-cell level investigated by confocal Raman microspectroscopy*. *Analyst*, 2009. **134**(6): p. 1149-53.
13. Kirschner, C., et al., *Monitoring of denaturation processes in aged beef loin by Fourier transform infrared microspectroscopy*. *J Agric Food Chem*, 2004. **52**(12): p. 3920-9.
14. Wartewig, S. and R.H. Neubert, *Pharmaceutical applications of Mid-IR and Raman spectroscopy*. *Adv Drug Deliv Rev*, 2005. **57**(8): p. 1144-70.
15. Roggo, Y., et al., *Infrared hyperspectral imaging for qualitative analysis of pharmaceutical solid forms*. *Anal Chim Acta*, 2005. **535**(1-2): p. 79-87.
16. Vajna, B., et al., *Testing the performance of pure spectrum resolution from Raman hyperspectral images of differently manufactured pharmaceutical tablets*. *Analytica Chimica Acta*, 2012. **712**: p. 45-55.
17. Lewis, E.N., E. Lee, and L.H. Kidder, *Combining Imaging and Spectroscopy: Solving Problems with Near Infrared Chemical Imaging*. *Microscopy Today*, 2004. **12**(6): p. 8-12.
18. Schlücker, S., et al., *Raman microspectroscopy: a comparison of point, line, and wide-field imaging methodologies*. *Anal Chem*, 2003. **75**(16): p. 4312-8.
19. Rogalski, A., *Optical detectors for focal plane arrays*. *OptoElectronics Review*, 2004. **12**(2): p. 221-245.

20. Lasch, P., *Spectral pre-processing for biomedical vibrational spectroscopy and microspectroscopic imaging*. Chemom Intell. Lab Syst., 2012(in press).
21. Lasch, P., et al., *Imaging of colorectal adenocarcinoma using FT-IR microspectroscopy and cluster analysis*. Biochim Biophys Acta, 2004. **1688**(2): p. 176-86.
22. Chernenko, T., et al., *Label-free Raman spectral imaging of intracellular delivery and degradation of polymeric nanoparticle systems*. ACS Nano, 2009. **3**(11): p. 3552-9.
23. Hedegaard, M., et al., *Spectral unmixing and clustering algorithms for assessment of single cells by Raman microscopic imaging*. Theoretical Chemistry Accounts: Theory, Computation, and Modeling (Theoretica Chimica Acta), 2011. **130**(4): p. 1249-1260.
24. Bergner, N., et al., *Unsupervised unmixing of Raman microspectroscopic images for morphochemical analysis of non-dried brain tumor specimens*. Anal Bioanal Chem, 2012. **403**(3): p. 719-25.
25. Lasch, P., et al., *Artificial neural networks as supervised techniques for FT-IR microspectroscopic imaging*. J Chemom, 2007. **20**(5): p. 209-220.
26. Kneipp, K., *Surface-enhanced Raman scattering*. Physics Today, 2007. **11**: p. 40-46.
27. Alexandrov, T., et al., *Spatial segmentation of imaging mass spectrometry data with edge-preserving image denoising and clustering*. J Proteome Res, 2010. **9**(12): p. 6535-6546.
28. Grasmair, M., *Locally Adaptive Total Variation Regularization*. Scale Space and Variational Methods in Computer Vision, Proceedings, 2009. **5567**: p. 331-342.
29. Rudin, L., S. Osher, and E. Fatemi, *Nonlinear total variation based noise removal algorithms*. Proceedings of the eleventh annual international conference of the Center for Nonlinear Studies on Experimental mathematics : computational issues in nonlinear science: computational issues in nonlinear science, 1992. **60**(1-4): p. 259-268.
30. Chambolle, A. and A. Kokaram, *An Algorithm for Total Variation Minimization and Applications*. Journal of Mathematical Imaging and Vision, 2004. **20**(1): p. 89-97.
31. MacQueen, J. *Some methods for classification and analysis of multivariate observations*. in *Proc. Fifth Berkeley Symp. on Math. Statist. and Prob.* 1967: Univ. of Calif. Press.
32. Lasch, P., A. Hermelink, and D. Naumann, *Correction of axial chromatic aberrations in confocal Raman microspectroscopic measurements of a single microbial spore*. Analyst, 2009. **134**(6): p. 1162-70.
33. Hedegaard, M., et al., *Discriminating isogenic cancer cells and identifying altered unsaturated fatty acid content as associated with metastasis status, using k-means clustering and partial least squares-discriminant analysis of Raman maps*. Anal Chem, 2010. **82**(7): p. 2797-802.
34. Mizuno, A., et al., *Near-infrared FT-Raman spectra of the rat brain tissues*. Neurosci Lett, 1992. **141**(1): p. 47-52.
35. Krafft, C., et al., *Near infrared Raman spectra of human brain lipids*. Spectrochim Acta A Mol Biomol Spectrosc, 2005. **61**(7): p. 1529-35.
36. Olsson, N.U., et al., *High-performance liquid chromatography method with light-scattering detection for measurements of lipid class composition: analysis of brains from alcoholics*. J Chromatogr B Biomed Appl, 1996. **681**(2): p. 213-8.
37. Carrie, I., et al., *Specific phospholipid fatty acid composition of brain regions in mice. Effects of n-3 polyunsaturated fatty acid deficiency and phospholipid supplementation*. J Lipid Res, 2000. **41**(3): p. 465-72.

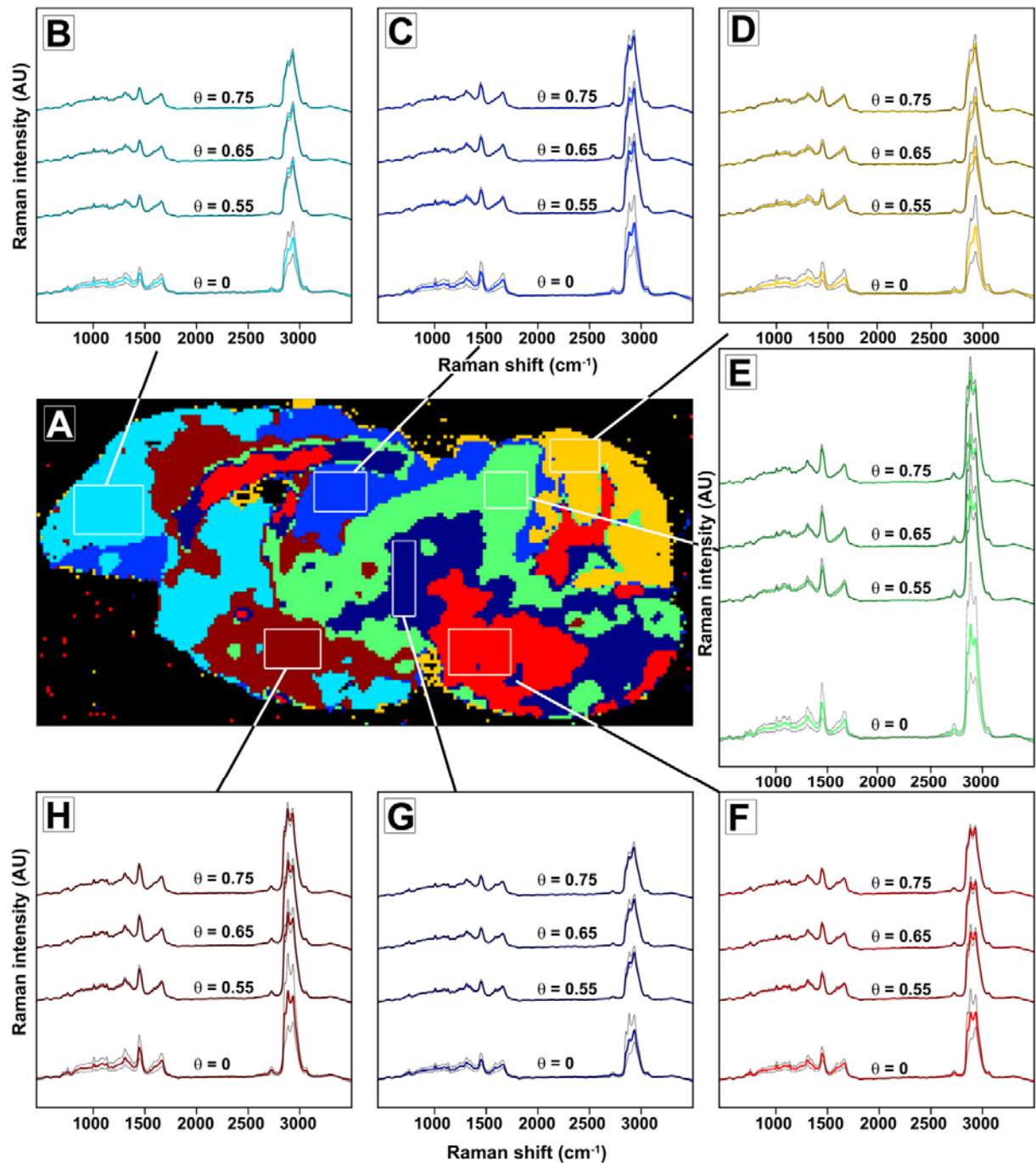
38. Rousseeuw, P., *Silhouettes: A graphical aid to the interpretation and validation of cluster analysis*. Journal of Computational and Applied Mathematics, 1987. **20**(1): p. 53-65.
39. Naumann, D., *FT-Infrared and FT-Raman Spectroscopy in Biomedical Research*. Applied Spectroscopy Reviews, 2001. **36**(2-3): p. 239-298.
40. Tantipolphan, R., et al., *Analysis of lecithin-cholesterol mixtures using Raman spectroscopy*. Journal of pharmaceutical and biomedical analysis, 2006. **41**(2): p. 476-84.
41. Byrne, H., G. Sockalingum, and N. Stone, *Raman Spectroscopy: Complement or Competitor?*, in *Biomedical Applications of Synchrotron Infrared Microspectroscopy*, D. Moss, Editor. 2011, Royal Society of Chemistry, RCS Analytical Spectroscopy Monographs: Cambridge. p. 105-142.

Table of Contents Graphic (for TOC only):





Supporting Figure S1. Data analysis workflow for hyperspectral image (HSI) segmentation of confocal Raman microspectroscopic data on the basis of edge-preserving denoising (EPD) and k-means cluster (KMC) analysis (see text for details). Blue rectangles denote the output of the EPD algorithm providing an improved interpretation of the Raman HSI dataset.



Supporting Figure S2. The influence of the degree of EPD on the Raman spectroscopic properties of manually defined regions of interest (ROIs). (A) Segmentation map according to Fig. 3C (moderate EPD, $\theta=0.65$). (B-H) Mean, 5th and 95th percentile spectra obtained from confocal Raman spectra of 7 selected rectangular regions of the mid-sagittal hamster brain

section (see inset of panel A). Confocal Raman spectra have been pre-processed in the spectral (quality test and cosmic ray removal, only) and spatial (for EPD level see inset) domains. The color coding is consistent with figures 2-4. Raman spectra were shifted along the y-axis for clarity.